Metamagnetic transition and a loss of magnetic hysteresis caused by electron trapping in monolayers of single-molecule magnet $Tb_2@C_{79}N$

Emmanouil Koutsouflakis,[1] Denis Krylov,[1,a] Nicolas Bachellier,[2] Daria Sostina,[2,b] Vasilii Dubrovin,[1] Fupin Liu,[1] Lukas Spree,[1] Georgios Velkos,[1] Sebastian Schimmel,[1,c] Yaofeng Wang,[1] Bernd Büchner,[1] Rasmus Westerström,[3,4] Claudiu Bulbucan,[3,4] Kyle Kirkpatrick,[5] Matthias Muntwiler,[2] Jan Dreiser,[2] Thomas Greber[2,5] Stas M. Avdoshenko,[1] Harry Dorn,[5] Alexey A. Popov[1]*

Supporting Information

Selected low-T STM topographies of $Tb_2@C_{79}N$ on Cu(111)

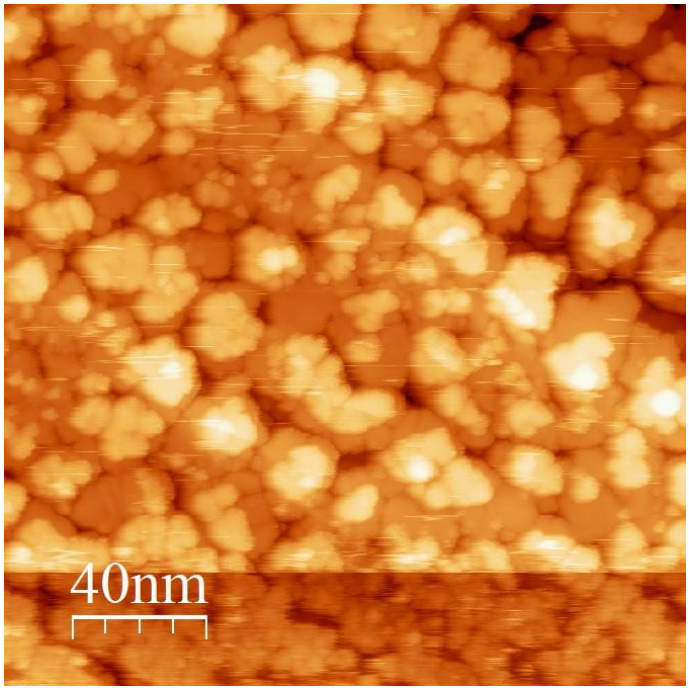

Figure S1. STM topography of multilayer $Tb_2@C_{79}N$ on Cu(111) (studied then by XPS). Measurement parameters: U = 0.8 V, I = 20 pA, T = 4.8 K.

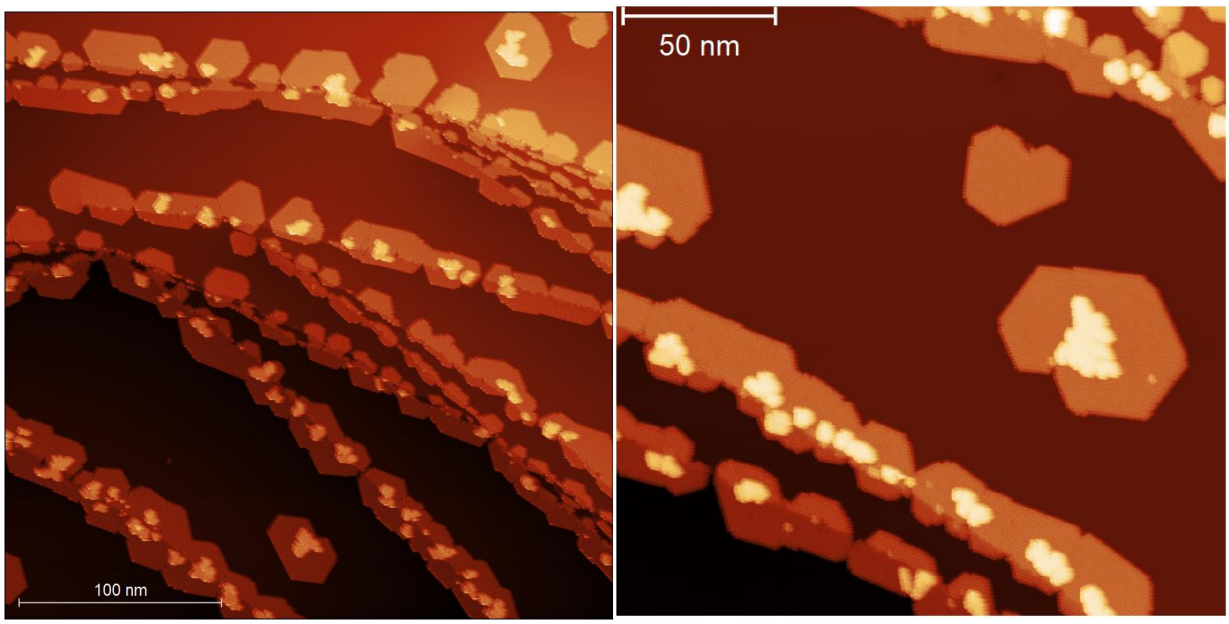

Figure S2. $Tb_2@C_{79}N$ submonolayer on Cu(111) (studied then by XPS). Measurement parameters: U = 1 V, I = 20 pA (left); U = 0.8 V, I = 50 pA (right), T = 4.8 K.

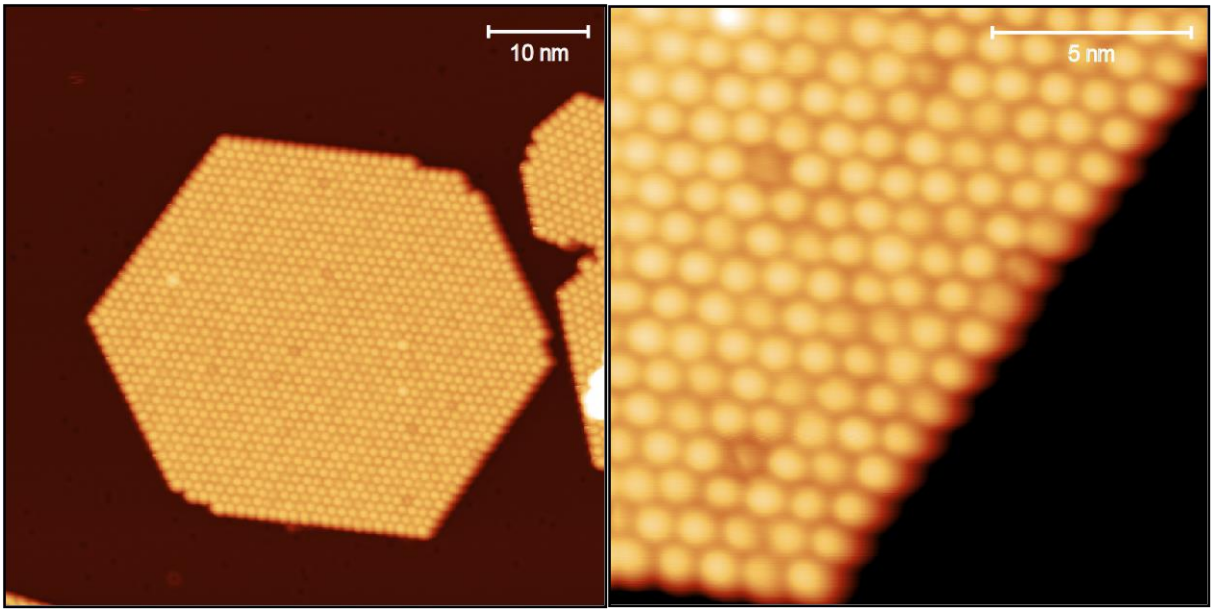

Figure S3. $Tb_2@C_{79}N$ on Cu(111). Measurement parameters: U = 0.8 V, I = 20 pA, T = 4.8 K.

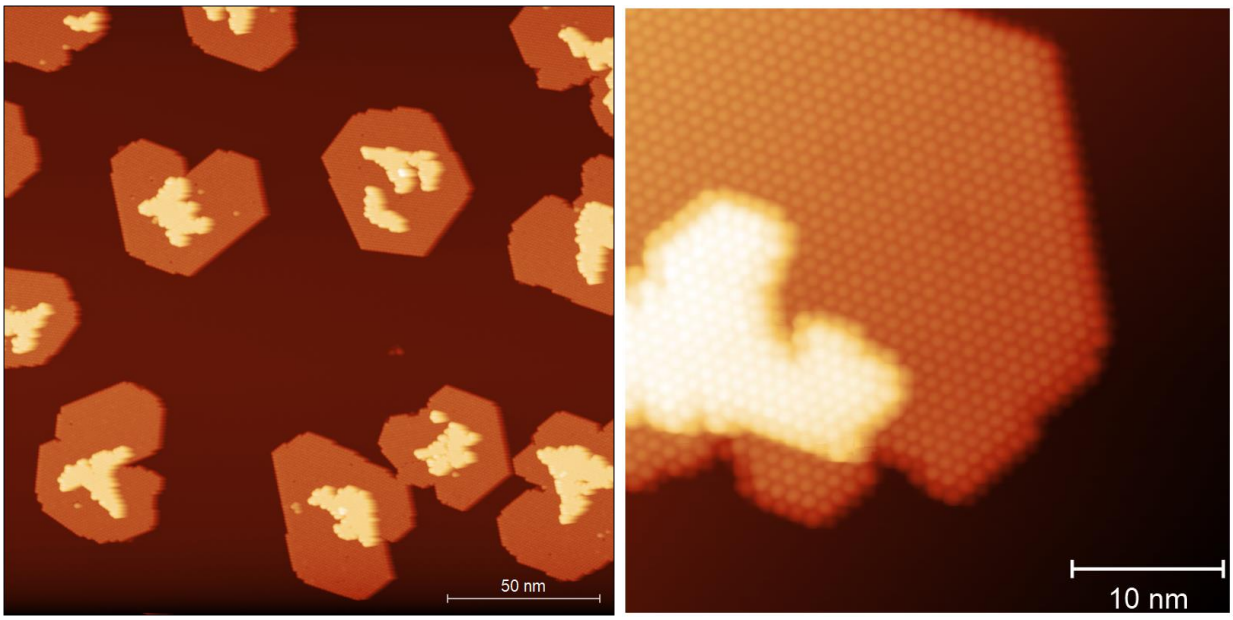

Figure S4. $Tb_2@C_{79}N$ on Cu(111). Measurement parameters: U = 1 V, I = 20 pA (left), U = 0.8 V, I = 50 pA (right) T = 4.8 K.

STS studies of $Tb_2@C_{79}N$ on Cu(111): first layer

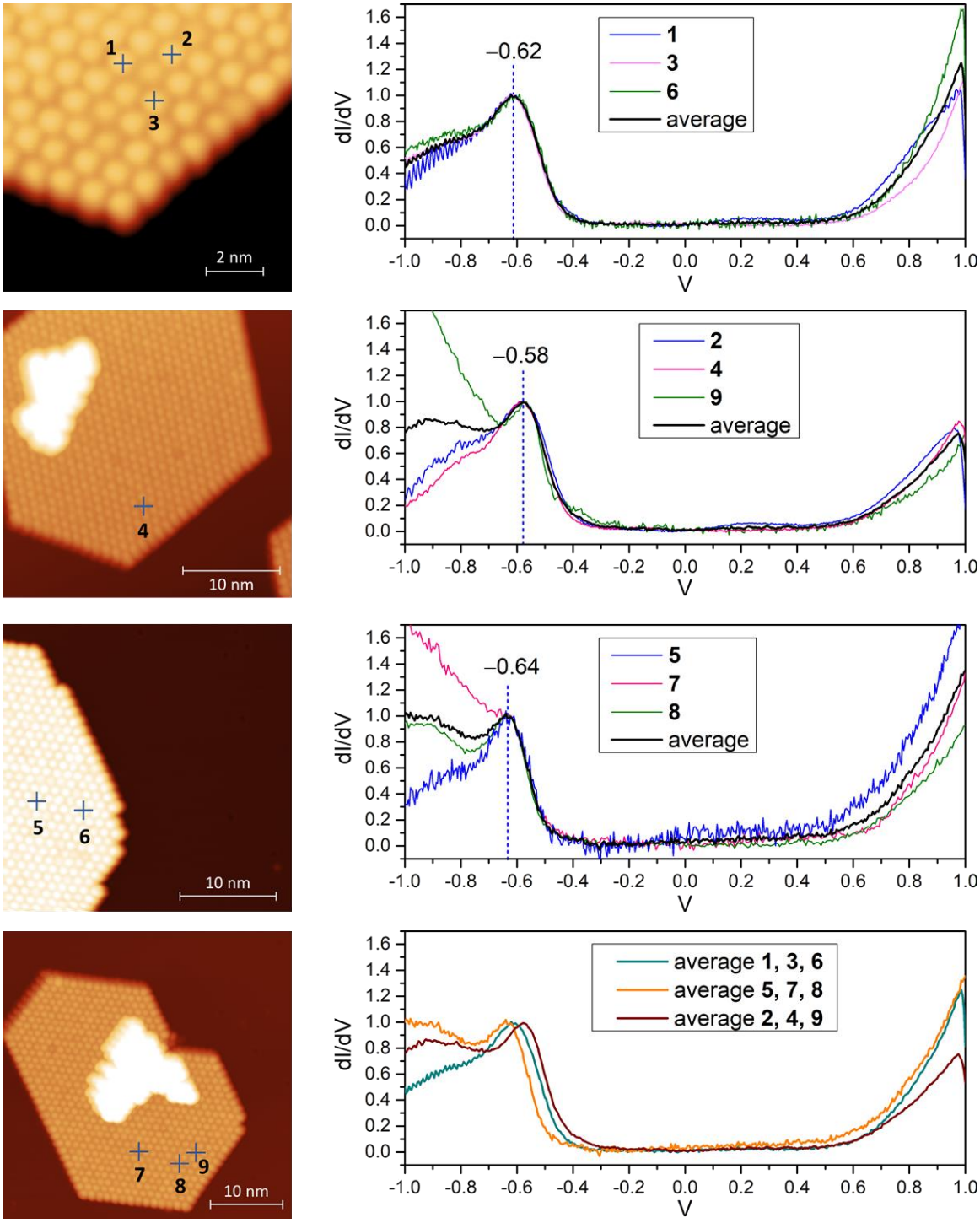

Figure S5. Left: STM topographies of $Tb_2@C_{79}N$ islands on Cu(111) with positions, at which STS measurements were done (U = 0.8 V, I = 20 pA). Right: *dI/dU* curves measured over monolayer regions. The curves are grouped according to HOMO peak position. The bottom panel shows averaged curve for each group. T = 4.8 K

STS studies of $Tb_2@C_{79}N$ on Cu(111): second layer

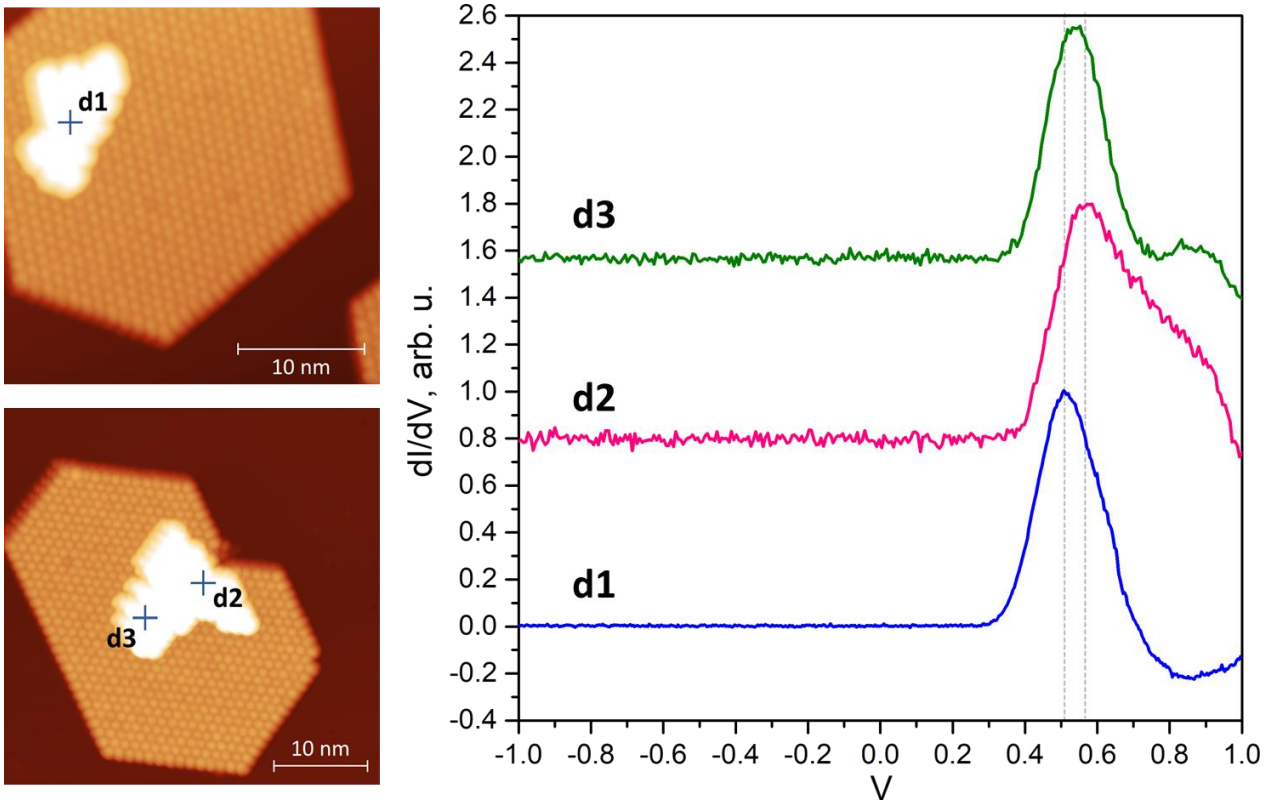

Figure S6. Left: STM topographies of $Tb_2@C_{79}N$ islands on Cu(111) with positions, at which STS measurements were done. Right: *dI/dU* curves measured over double-layer regions. T = 4.8 K

Selected low-T STM topographies of $Tb_2@C_{79}N$ on Au(111)

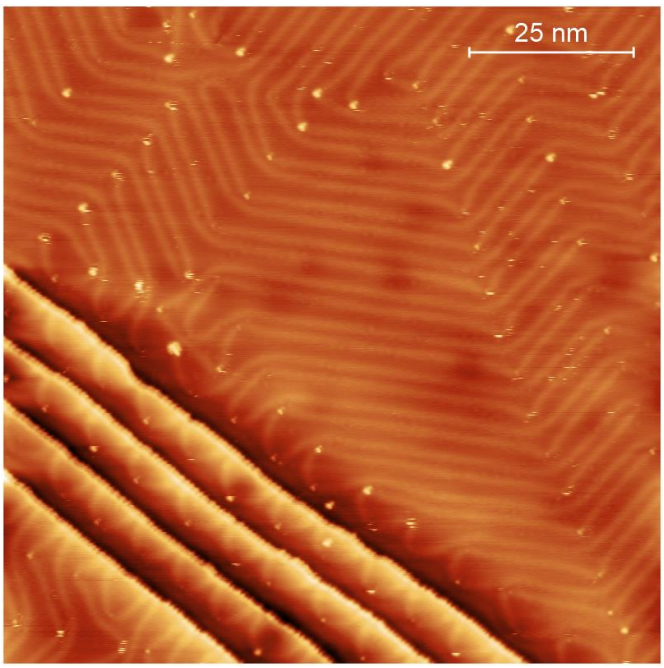

Figure S7. Low-T STM topography of Au(111) before deposition of fullerenes. *T* = 4.8 K. Left: *U* = −0.5 V, *I* = 100 pA.

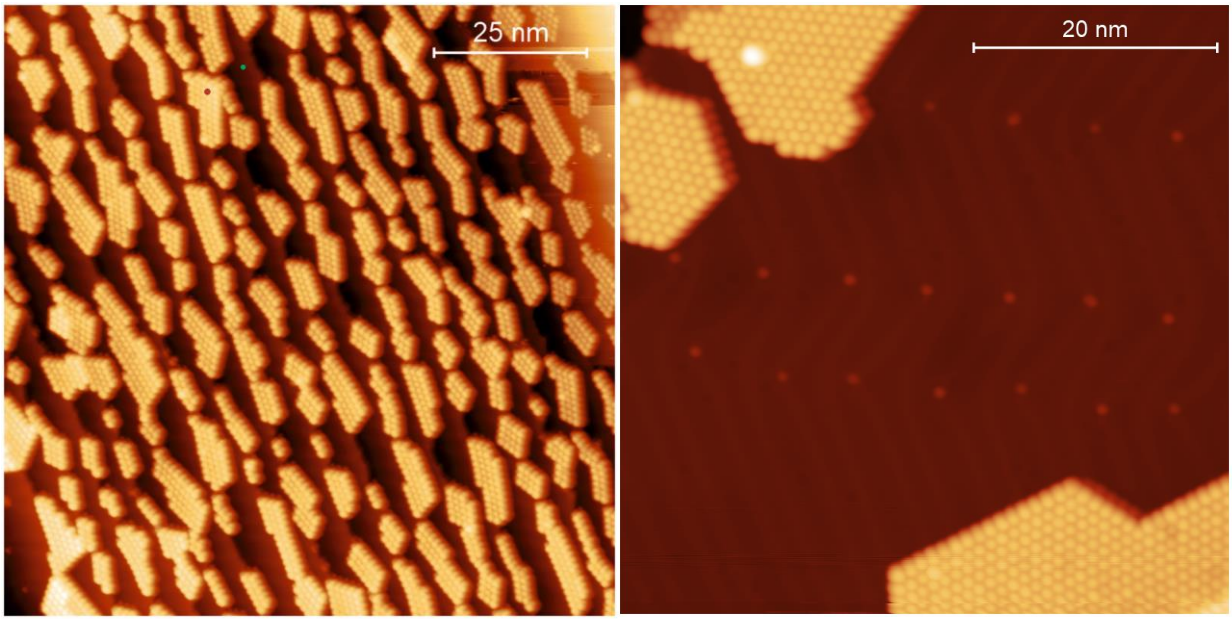

Figure S8. Low-T STM topographies of $Tb_2@C_{79}N$ on Au(111). *T* = 4.8 K. Left: *U* = 0.6 V, *I* = 20 pA. Right: *U* = 1 V, *I* = 20 pA.

STS studies of $Tb_2@C_{79}N$ on Au(111)

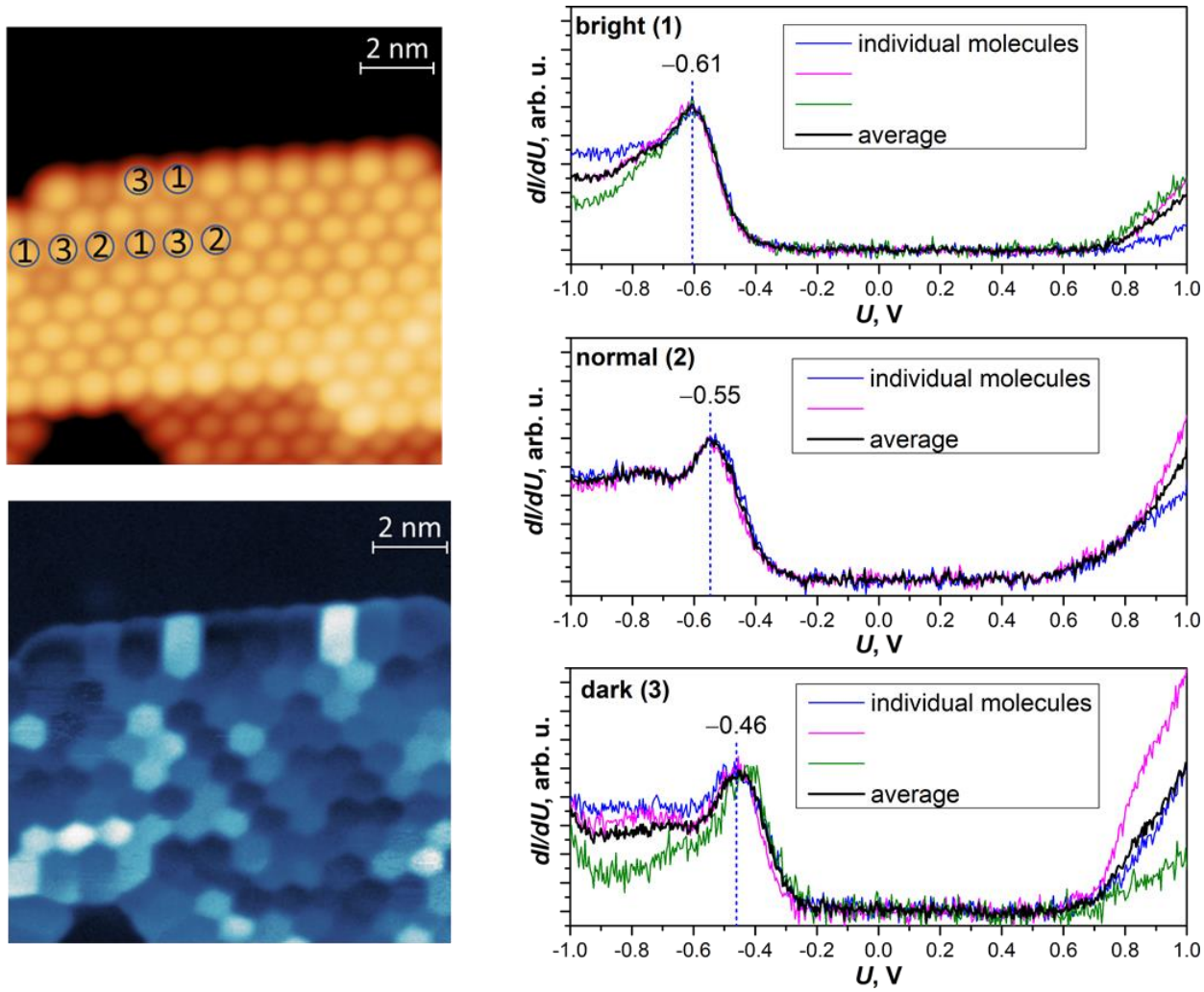

Figure S9a. STS curves measured over different molecules in $Tb_2@C_{79}N$ monolayer island on Au(111) and averaged curves in three groups (with different brightness in the *dI/dU* map). Curves are normalized to the HOMO peak intensity. STM topography and *dI/dU* map of the same island at the bias voltage $U = -0.632$ V are shown on the left. Numbers on the molecules correspond to three types (1 – bright, 2 – normal, 3 – dark). $T = 4.8$ K.

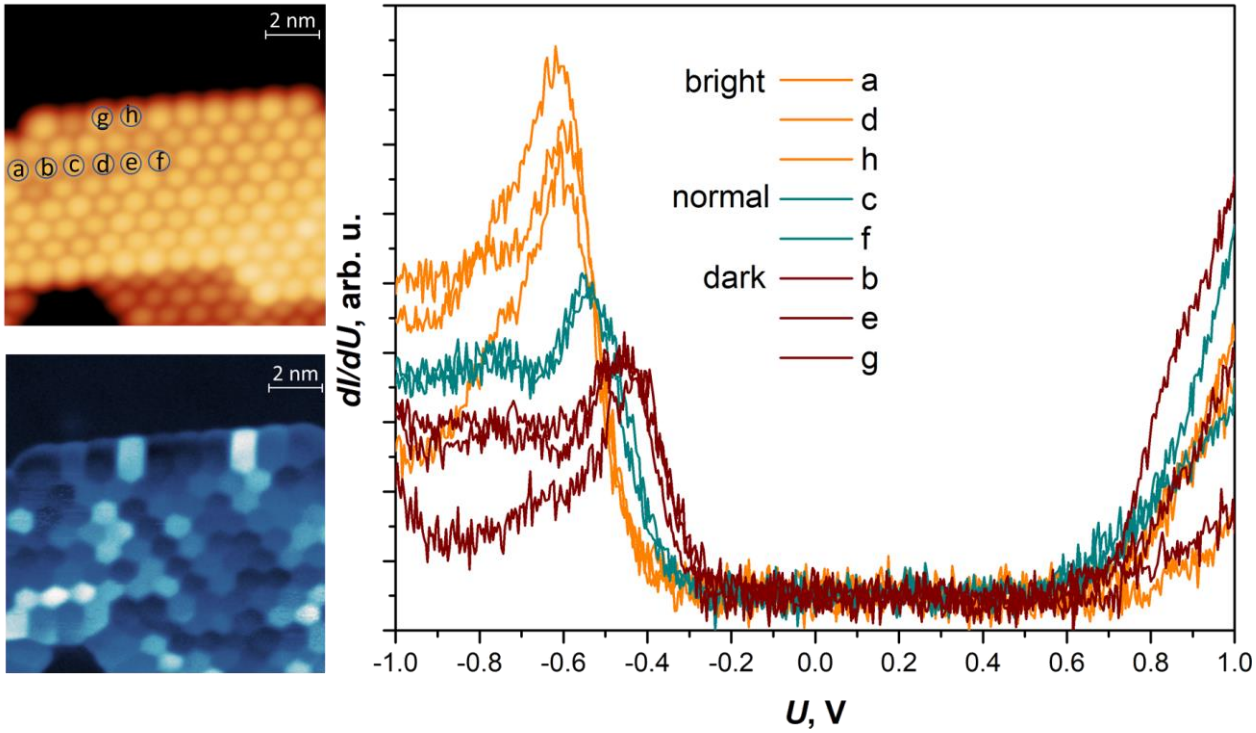

Figure S9b. Non-normalized STS curves measured over different molecules in $Tb_2@C_{79}N$ monolayer island on Au(111) (the same as in Fig. S9a; different colors corresponds to different brightness in the *dI/dU* map). STM topography with labeling of molecules and *dI/dU* map of the same island at the bias voltage U = −0.632 V are shown on the left.

STM topographies of $Tb_2@C_{79}N$ on Au(111) and Cu(111) for samples used in XMCD studies

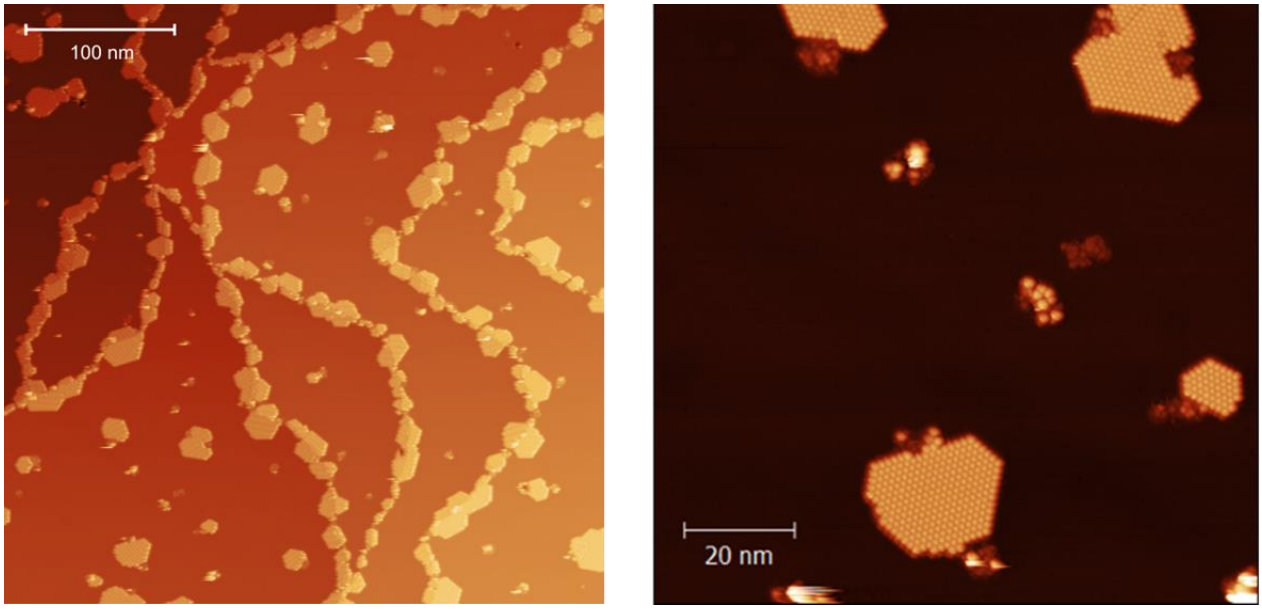

Figure S10. STM topographies of the $Tb_2@C_{79}N$ submonolayer on Cu(111) used in XMCD measurements. Room temperature, U = 1 V, I = 20 pA.

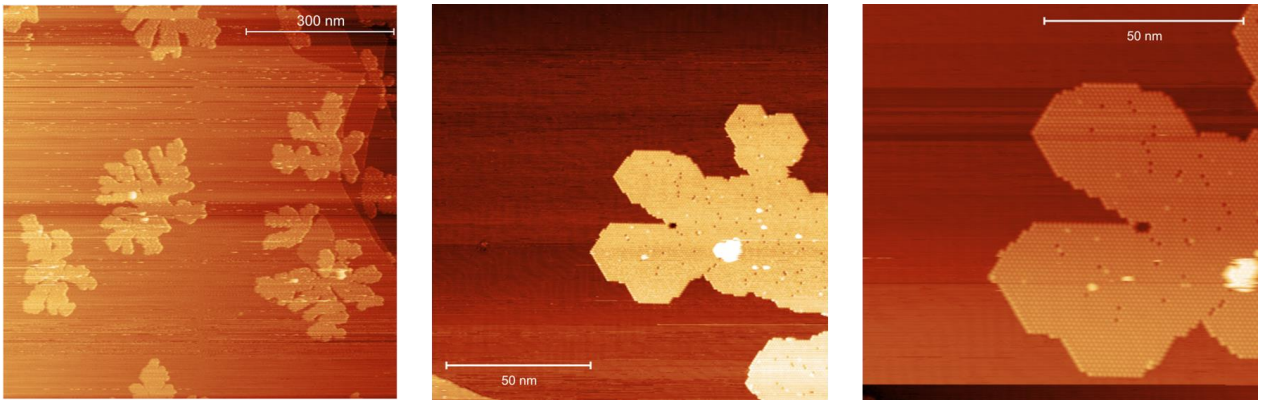

Figure S11. STM topographies of the $Tb_2@C_{79}N$ submonolayer on Au(111) used in XMCD measurements. Room temperature, U = 1 V, I = 250 pA (left); U = 0.7 V, I = 100 pA (middle); U = 0.7 V, I = 800 pA (right).

Relative energies of different $Tb_2@C_{79}N$ configurations on different substrates

To model geometrical configuration of $Tb_2@C_{79}N$ molecule on surface, one needs to consider very different orientation of the endohedral Tb_2 dimer, and, simultaneously, different positions of nitrogen atoms. In our previous works, we showed that Fibonacci sampling (logarithmic spiral indexes along z-axis) with 120 nodes provides a sufficient sampling for a single parameter space (i.e. when only cluster orientation is controlled).[1-3] For $Tb_2@C_{79}N$ molecule on a given substrate surface, with two parameters to control (φ(Tb_2–*z*) and θ(N–CM–*z*), see Fig. 5a and Fig. S12), the number of compositions grows rapidly. For example, with only 10 grid points along two degrees of freedom one has 100 systems to consider and this grid is not even dense enough. One way to reduce the number of geometrical points and still have vast and homogenous sampling is independently moving along grid points. It is straightforward to realize in 2D, where the cluster and nitrogen are locked to one plane. With φ and θ changing from 0 to π clockwise (N) and anti-clockwise (Tb_2 dimer), respectively, for every given number of grid points, φ and θ will have homogenous sampling, while hybrid (φ, θ)-pair will have a fair representation. Although such sampling is incomplete, it is better than just a random sampling on the same 10 points. To have this idea expand towards (φ(Tb_2–*z*), θ(N–CM–*z*)) sampling for systems in 3D, we allow the Tb_2 dimer axis and nitrogen to move along grid points of Fibonacci 120 nodes. Combination with independently moving N-site in two orthogonal directions to the cluster such logarithmic spiral gives immeasurable coverage of parametric space for the given 240 points. Figure S12 shows relative energies of different configurations plotted versus φ(Tb_2–*z*) and θ(N–CM–*z*) values.

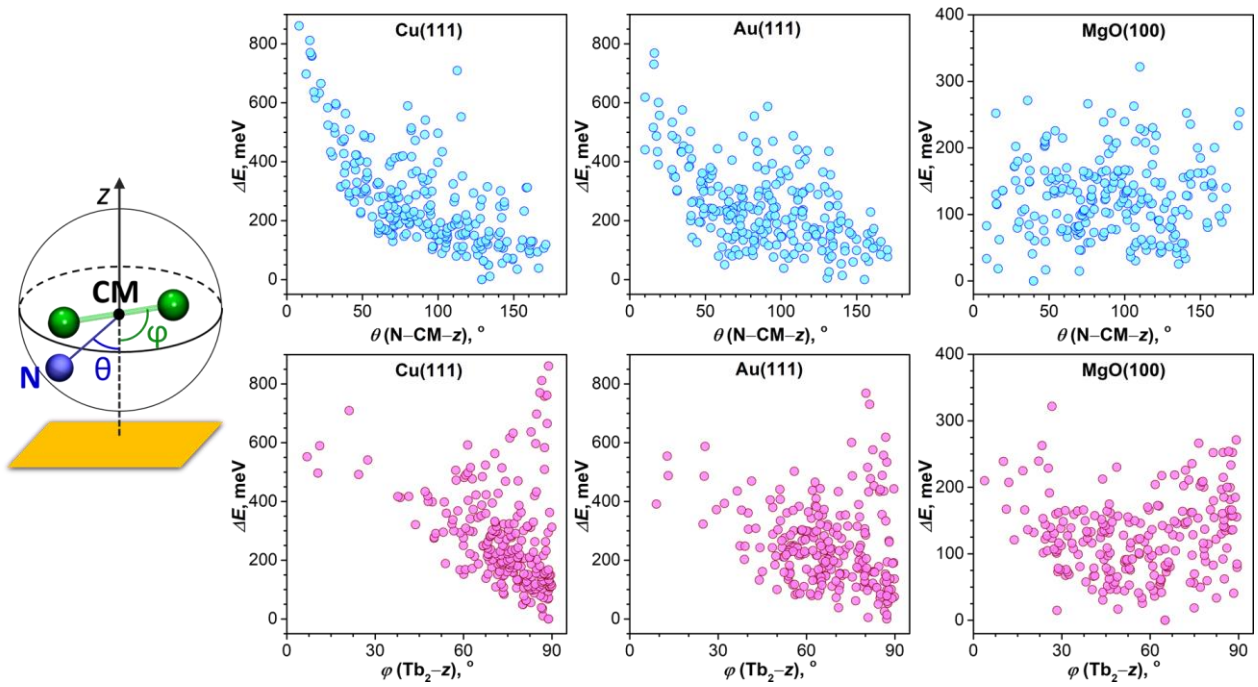

Figure S12. DFT-computed relative energies of different $Tb_2@C_{79}N$ configurations on Cu(111), Au(111), and MgO(100) as a function of φ(Tb_2–*z*) and θ(N–CM–*z*) angles. Definition of the angles is shown on the left, CM is the center of mass, z is a normal to the surface.

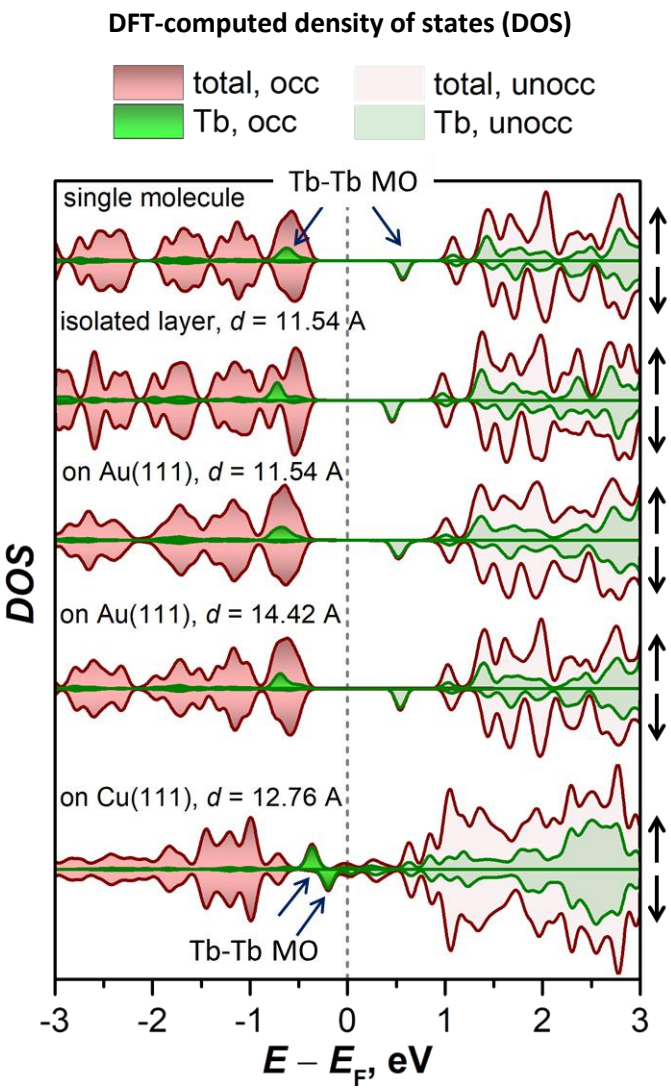

Figure S13. DFT-computed electron density of states for $Tb_2@C_{79}N$ as isolated molecule and in weakly-interacting layer (intermolecular distance *d* = 11.54 Å), as a layer on Au(111) with two intermolecular distances (11.54 Å and 14.42 Å), and as a layer on Cu(111) with *d* = 12.76 Å. Note that Tb–Tb bonding MO is singly occupied in an isolated molecule and in $Tb_2@C_{79}N$ absorbed on Au(111), but is two-fold occupied on Cu(111).

Charge redistribution after absorption of $Tb_2@C_{79}N$ molecule

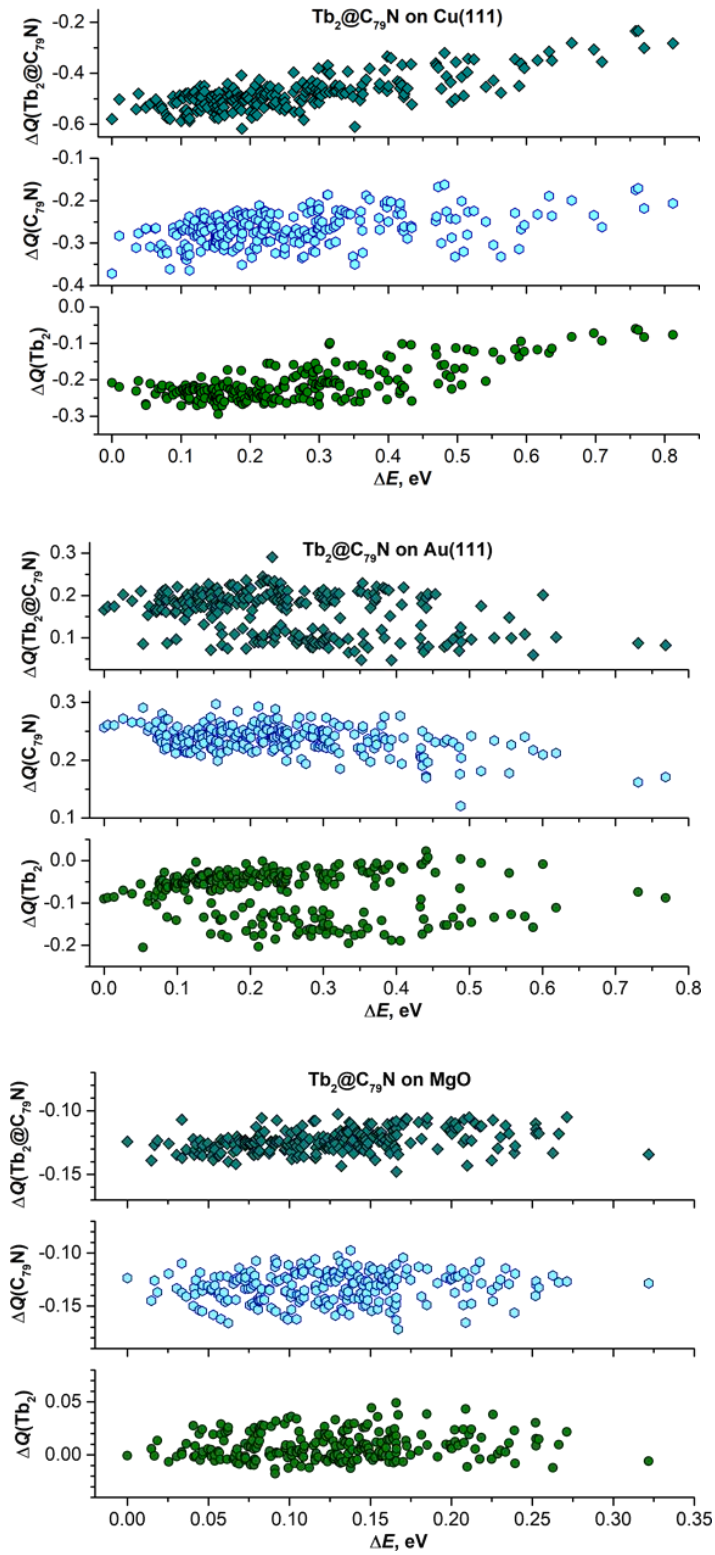

Figure S14. Changes of Bader charges ΔQ of the whole $Tb_2@C_{79}N$ molecule as well as its fullerene cage ($C_{79}N$) and endohedral metal dimer (Tb_2) after deposition on a substrate for all computed structures (240 in each set). The data are sorted according to the relative energy of a given landing configuration.

Difference and spin density of $Tb_2@C_{79}N$ on Cu(111) and Au(111)

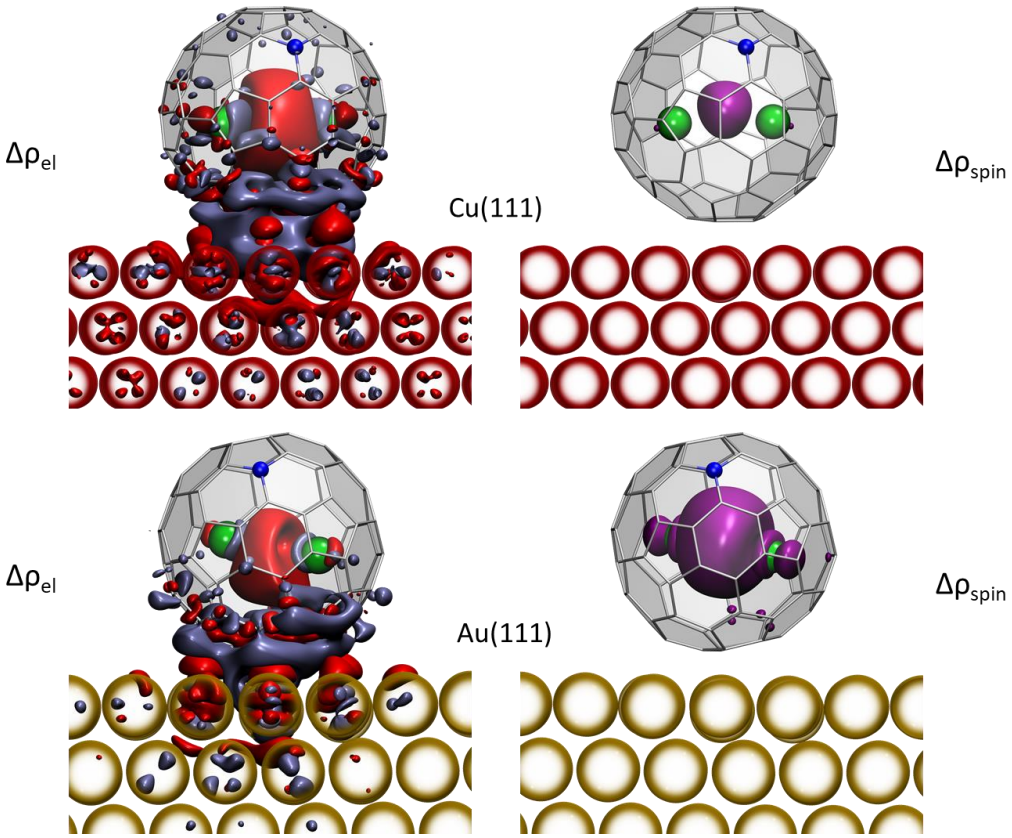

Figure S15. Difference electron density ($\Delta\rho_{el}$) and spin density ($\Delta\rho_{spin}$) for $Tb_2@C_{79}N$ adsorbed on Cu(111) and Au(111). Note that the spin density for the molecule on Cu(111) is considerably lower than for the molecule on Au(111).

Magnetic hysteresis of drop-casted $Tb_2@C_{79}N$ multilayer on Au measured by XMCD

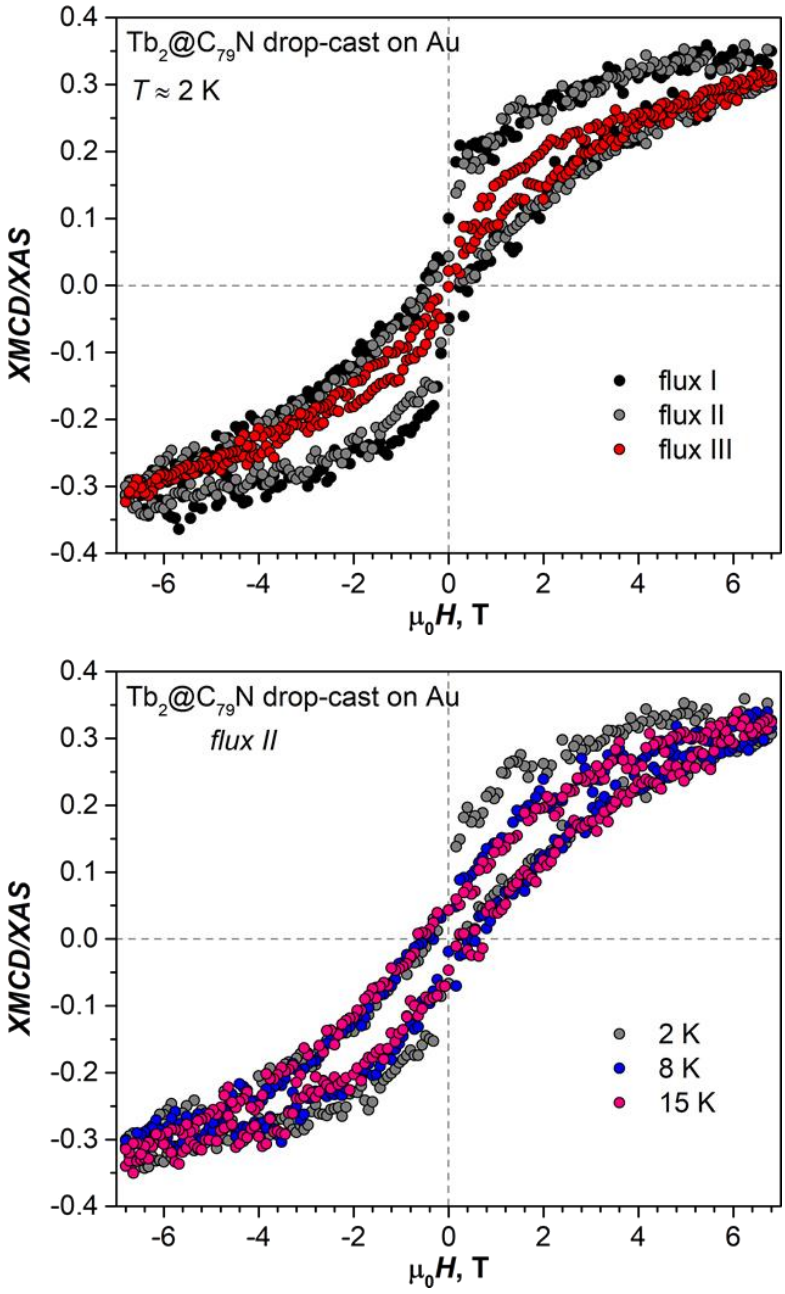

Figure S16. Top: magnetic hysteresis of $Tb_2@C_{79}N$ multilayer drop-casted on Au measured at T≈2 K with three different values of X-ray flux (I: 0.3 10^{-2}; II: 0.6 10^{-2}; III: 2 10^{-2} photons nm^{-2} sec^{-1}). Bottom: Magnetic hysteresis of $Tb_2@C_{79}N$ multilayer drop-casted on Au measured with flux II at different temperatures. Opening of the hysteresis after decrease of the flux from III to II and I and further preservation of the shape during variable-temperature measurements indicate that the sample does not undergo radiation damage.

The sample was prepared by drop-casting $Tb_2@C_{79}N$ solution in toluene on Au crystal and letting it dry under flow of nitrogen, giving microcrystalline film. Analogous procedure was used for preparing the $Tb_2@C_{79}N$ sample on quartz holder for SQUID measurements in Ref. 30 (the curve shown in Fig. 7a in the main text).

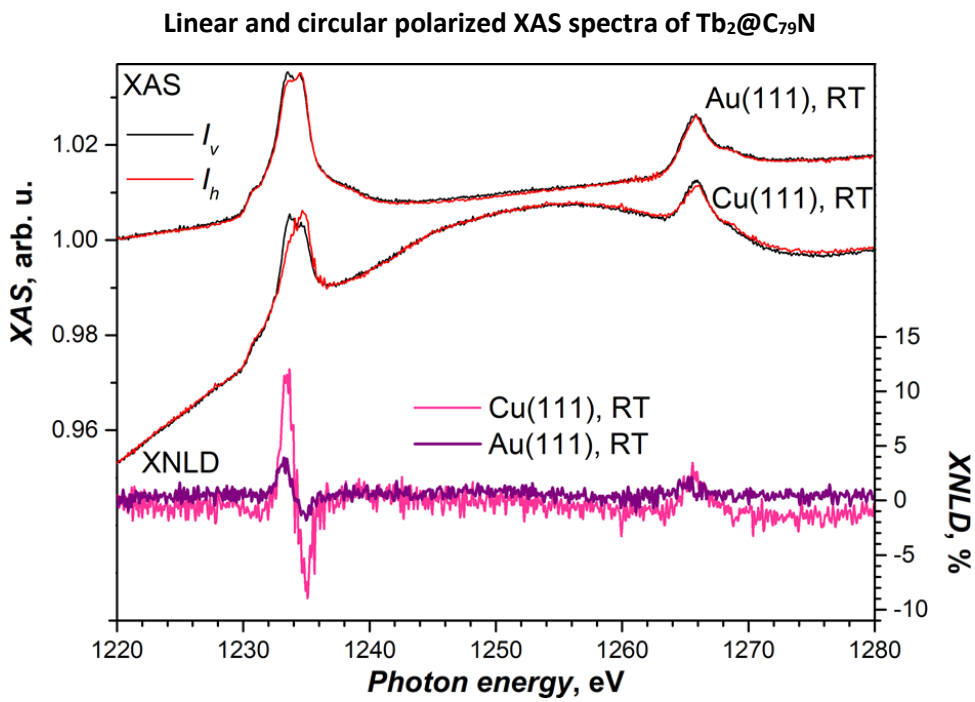

Figure S17. X-ray natural linear dichroism (XNLD) spectra of $Tb_2@C_{79}N$ layer on Au(111) and Cu(111) measured at room temperature. Grazing incidence of X-ray beam, I_v and I_h are X-ray absorption intensities for vertical (v) and horizontal (h) orientation of polarization, respectively.

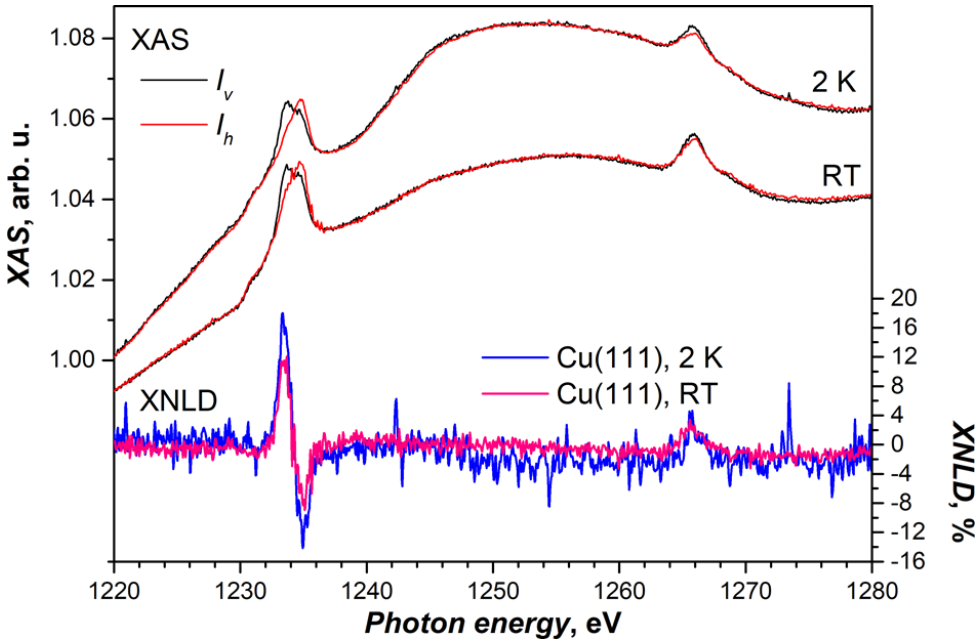

Figure S18. X-ray natural linear dichroism (XNLD) spectra of $Tb_2@C_{79}N$ layer on Cu(111) measured at room temperature and close to 2 K. Grazing incidence of X-ray beam, I_v and I_h are X-ray absorption intensities for vertical (v) and horizontal (h) orientation of polarization, respectively. Increase of the XNLD signal at low temperature may indicates that the motion of the Tb_2 unit and probably whole molecule is hampered leading to increased degree of ordering. Note that Cu has strong background in the same energy range, which affects the shape of the spectra and complicates numerical analysis.

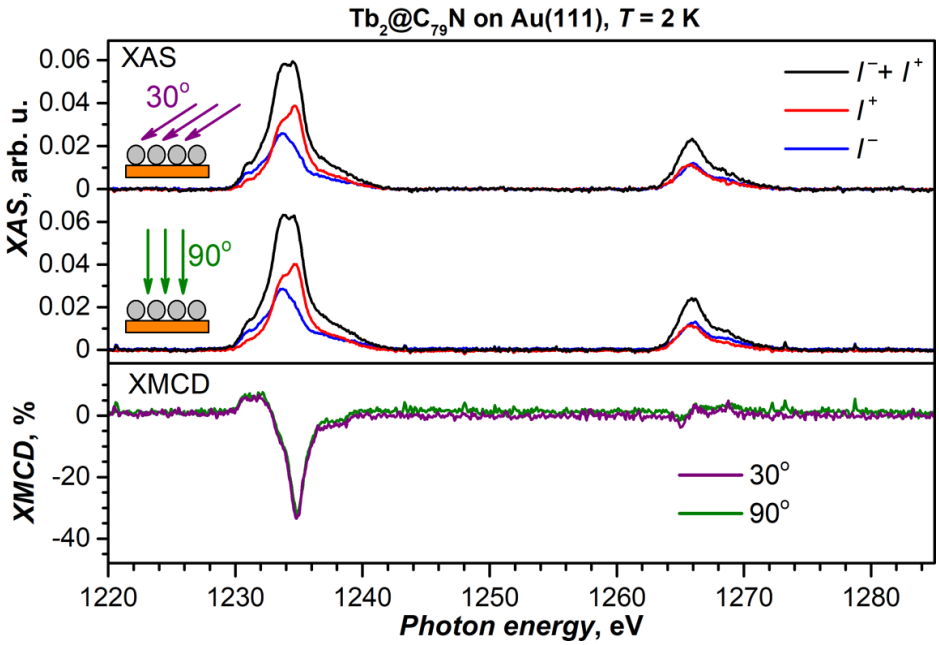

Figure S19. Tb-$M_{4,5}$ XAS (top panels) and XMCD (bottom panels) spectra of $Tb_2@C_{79}N$ evaporated onto on Au(111). $T \approx 2$ K, $\mu_0 H = 6.8$ T, grazing (30°) and normal (90°) X-ray and magnetic field incidence with respect to the surface.

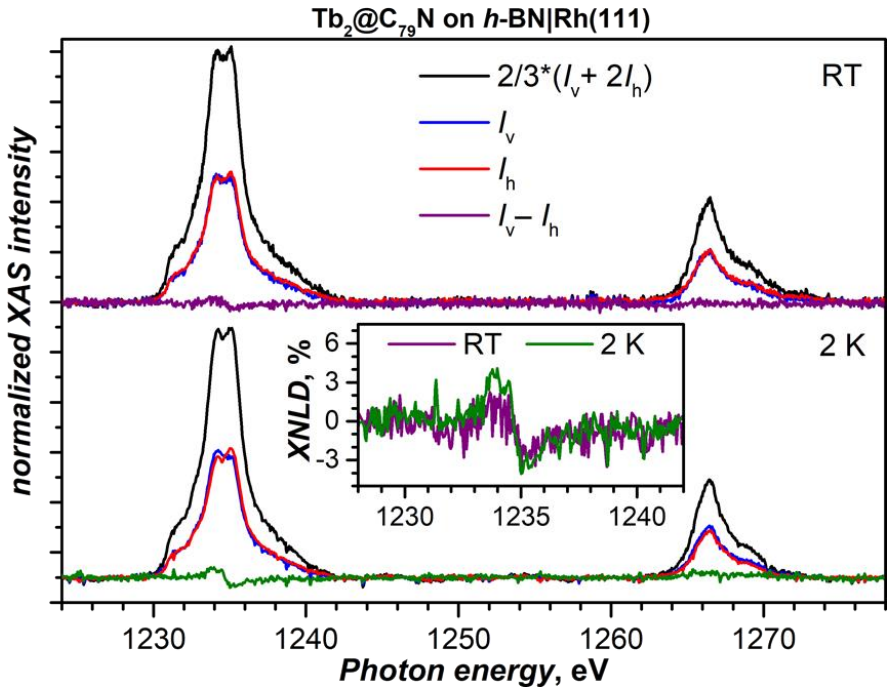

Figure S20. X-ray natural linear dichroism (XNLD) spectra of $Tb_2@C_{79}N$ layer on *h*-BN|Rh(111) measured at room temperature and close to 2 K, grazing incidence of X-ray beam. I_v and I_h are X-ray absorption intensities for vertical (v) and horizontal (h) orientation of polarization, respectively.

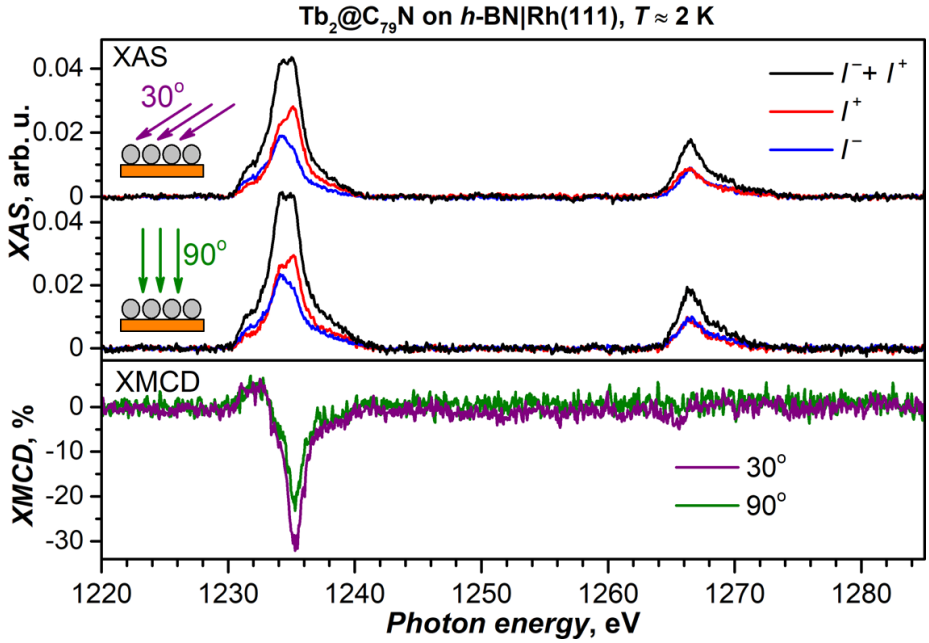

Figure S21. Tb-$M_{4,5}$ XAS (top panels) and XMCD (bottom panels) spectra of $Tb_2@C_{79}N$ evaporated onto on *h*-BN|Rh(111). $T \approx 2$ K, $\mu_0 H = 6.8$ T, grazing (30°) and normal (90°) X-ray and magnetic field incidence with respect to the surface.

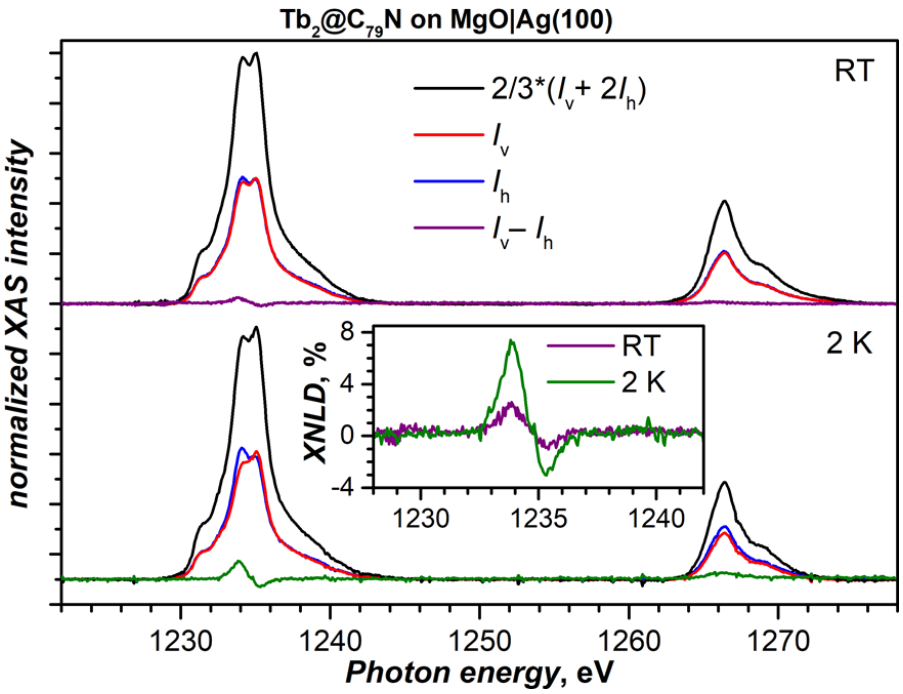

Figure S22. X-ray natural linear dichroism (XNLD) spectra of $Tb_2@C_{79}N$ layer on MgO|Ag(100) measured at room temperature and close to 2 K, grazing incidence of X-ray beam. I_v and I_h are X-ray absorption intensities for vertical (v) and horizontal (h) orientation of polarization, respectively. Increase of the XNLD signal at low temperature may indicates that the motion of the Tb_2 unit and probably whole molecule is hampered leading to increased degree of ordering.

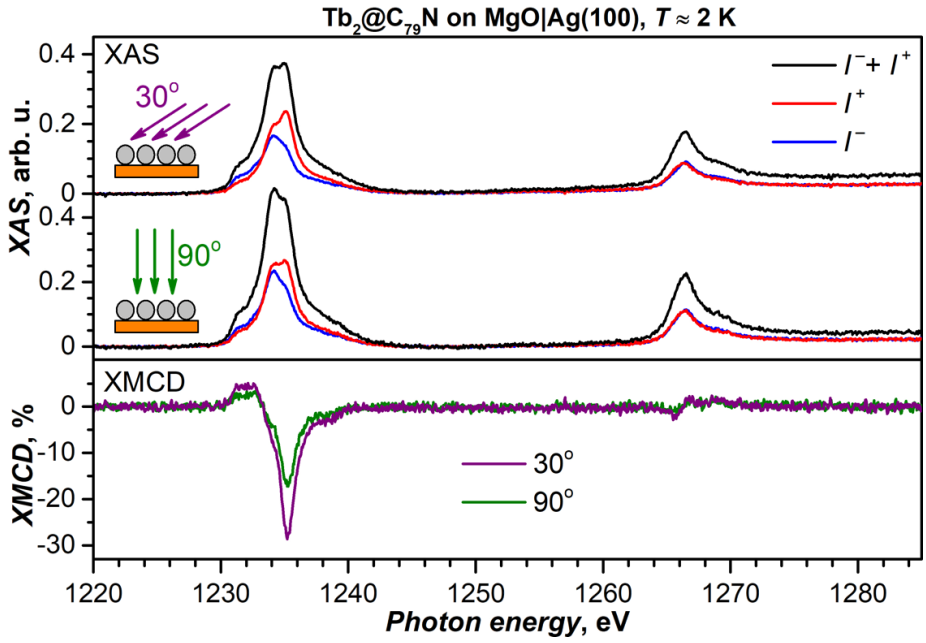

Figure S23. Tb-$M_{4,5}$ XAS (top panels) and XMCD (bottom panels) spectra of $Tb_2@C_{79}N$ evaporated onto MgO|Ag(100) (1.5 ML). $T \approx 2$ K, $\mu_0 H = 6.8$ T, grazing (30°) and normal (90°) X-ray and magnetic field incidence with respect to the surface.

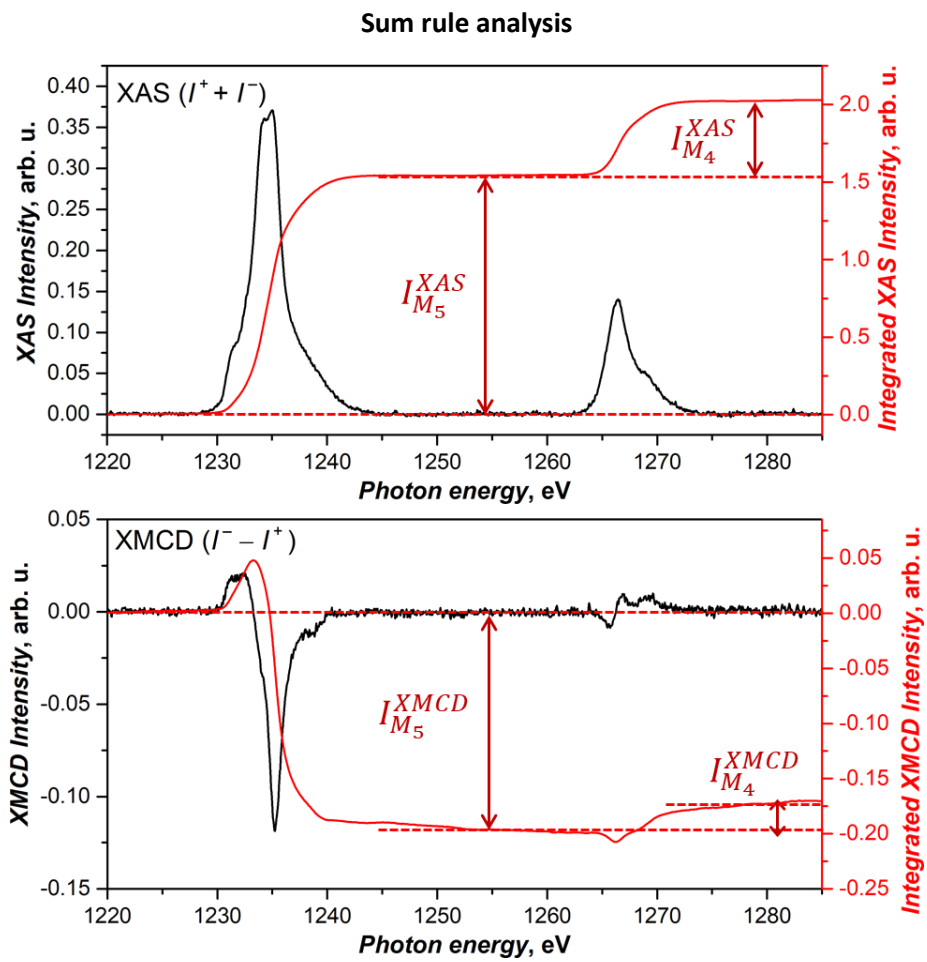

Figure S24. Example of the sum rule analysis for $Tb_2@C_{79}N$ evaporated onto MgO|Ag(100), T = 30 K, grazing incidence. Top and bottom panels show XAS and XMCD spectra at the Tb-$M_{4,5}$ edge together with integral curves (red). Definition of integrals used in calculations below is also shown on the figures.

Magnetic moment along direction of the beam, μ_z, can be calculated as $\mu_z = \left(\langle\hat{L}_z\rangle + 2\langle\hat{S}_z\rangle\right)\mu_B/\hbar$, where $\langle\hat{L}_z\rangle$ and $\langle\hat{S}_z\rangle$ are expectation values of angular and spin momentum operators. These values can be estimated from XAS and XMCD spectra using sum rules:[4, 5]

$$\langle\hat{L}_z\rangle = 3(14 - n_{4f})\frac{I_{M_5}^{XMCD} + I_{M_4}^{XMCD}}{3/2(I_{M_5}^{XAS} + I_{M_4}^{XAS})} \qquad \text{(Eq. S1a)}$$

$$\langle\hat{S}_z\rangle + 3\langle\hat{T}_z\rangle = 3/2(14 - n_{4f})\frac{I_{M_5}^{XMCD} - 3/2 I_{M_4}^{XMCD}}{3/2(I_{M_5}^{XAS} + I_{M_4}^{XAS})}\frac{1}{C_{\text{corr}}^{\text{Ln}}} \qquad \text{(Eq. S1b)}$$

Where n_{4f} is the number of 4f electrons (8 for Tb), integrals such as $I_{M_5}^{XAS}$ are defined in Figure S22, $\langle\hat{T}_z\rangle$ is the expectation values of spin dipole operator $\hat{T}_z$, and $C_{\text{corr}}^{\text{Ln}}$ is the correction factor from Ref. [6], which takes into account the deviation of the sum rules for spin momentum caused by partial mixing of $3d_{3/2}$ and $3d_{5/2}$ multiplets (for Tb^{3+}, the value is 0.882). $\langle\hat{S}_z\rangle$ can be determined from Eq. S1b using the relation $\langle\hat{T}_z\rangle/\langle\hat{S}_z\rangle = -0.083$ for Tb^{3+} tabulated in Ref. [6]. The uncertainty in determined μ_z is mainly caused by baseline ambiguities, especially for XMCD integrals, and is estimated to be 0.2–0.5 μ_B.

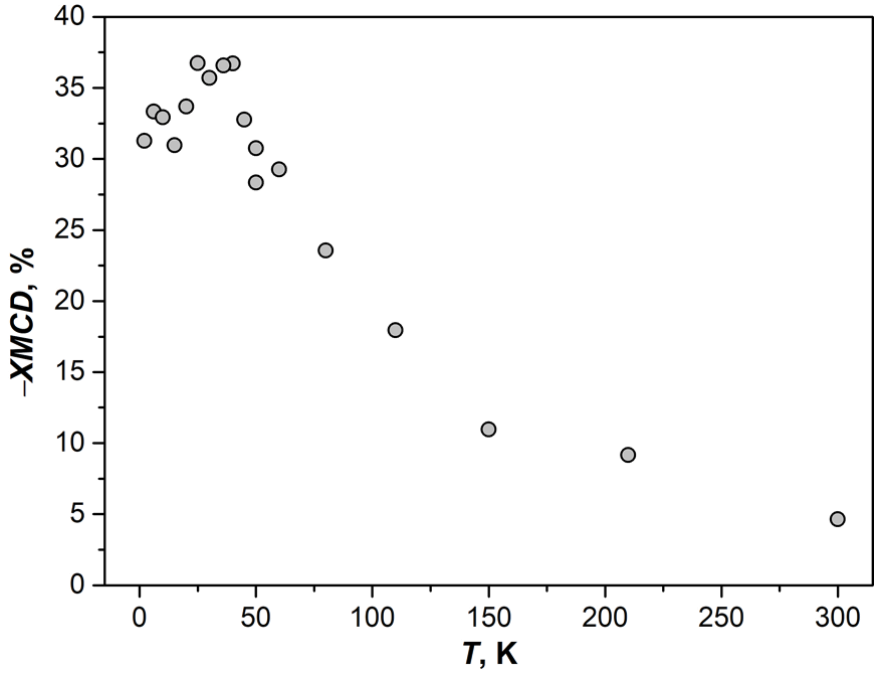

Figure S25. Temperature dependence of the XMCD signal intensity at Tb-M_5 edge in $Tb_2@C_{79}N$ submonolayer on *h*-BN|Rh(111). The data show the same trend as on MgO|Ag(100).

References

1. Krylov, D. S.; Schimmel, S.; Dubrovin, V.; Liu, F.; Nguyen, T. T. N.; Spree, L.; Chen, C.-H.; Velkos, G.; Bulbucan, C.; Westerström, R.; Studniarek, M.; Dreiser, J.; Hess, C.; Büchner, B.; Avdoshenko, S. M.; Popov, A. A., Substrate-independent magnetic bistability in monolayers of single molecule magnet $Dy_2ScN@C_{80}$ on metals and insulator. *Angew. Chem. Int. Ed.* **2020,** *59* (14), 5756-5764.
2. Velkos, G.; Krylov, D.; Kirkpatrick, K.; Spree, L.; Dubrovin, V.; Büchner, B.; Avdoshenko, S.; Bezmelnitsyn, V.; Davis, S.; Faust, P.; Duchamp, J.; Dorn, H.; Popov, A. A., High blocking temperature of magnetization and giant coercivity in the azafullerene $Tb_2@C_{79}N$ with a single-electron Tb–Tb bond. *Angew. Chem. Int. Ed.* **2019,** *58* (18), 5891-5896.
3. Dubrovin, V.; Gan, L.-H.; Büchner, B.; Popov, A. A.; Avdoshenko, S. M., Endohedral metal-nitride cluster ordering in metallofullerene–Ni^{II}(OEP) complexes and crystals: a theoretical study. *Phys. Chem. Chem. Phys.* **2019,** *21*, 8197-8200.
4. Thole, B. T.; Carra, P.; Sette, F.; van der Laan, G., X-ray circular dichroism as a probe of orbital magnetization. *Phys. Rev. Lett.* **1992,** *68* (12), 1943-1946.
5. Carra, P.; Thole, B. T.; Altarelli, M.; Wang, X., X-ray circular dichroism and local magnetic fields. *Phys. Rev. Lett.* **1993,** *70* (5), 694-697.
6. Teramura, Y.; Tanaka, A.; Thole, B. T.; Jo, T., Effect of Coulomb Interaction on the X-Ray Magnetic Circular Dichroism Spin Sum Rule in Rare Earths. *J. Phys. Soc. Jpn.* **1996,** *65* (9), 3056-3059.